

Chapter 6

ANALYSIS

INTRODUCTION

The data acquired using the broad-band pyrheliometer at Thule Air Base from May to October 1999 has been evaluated to reveal spectral aerosol optical depths. This information has subsequently been used to carry out the inversion procedure described in Chapter 4. The final results are of course dependent upon the quality of the optical depths used in the analysis. Considerable attention has therefore been devoted to accurate determinations of these quantities.

Data evaluation requires knowledge of ozone and nitrogen dioxide column amounts and the spectral cross sections of these species. Furthermore, atmospheric pressure and temperature at the observation site should be known. If the pyrheliometer response outside the atmosphere is sought, then a correction must be made for the current value of the extraterrestrial solar irradiance [Chapter 1, p 14].

An overview of the entire period of measurement (May 15th - October 4th, 1999) is available in Figure 6.1 showing the daily short wave radiant exposure incident upon a horizontal surface at the Thule Air Base laboratory.

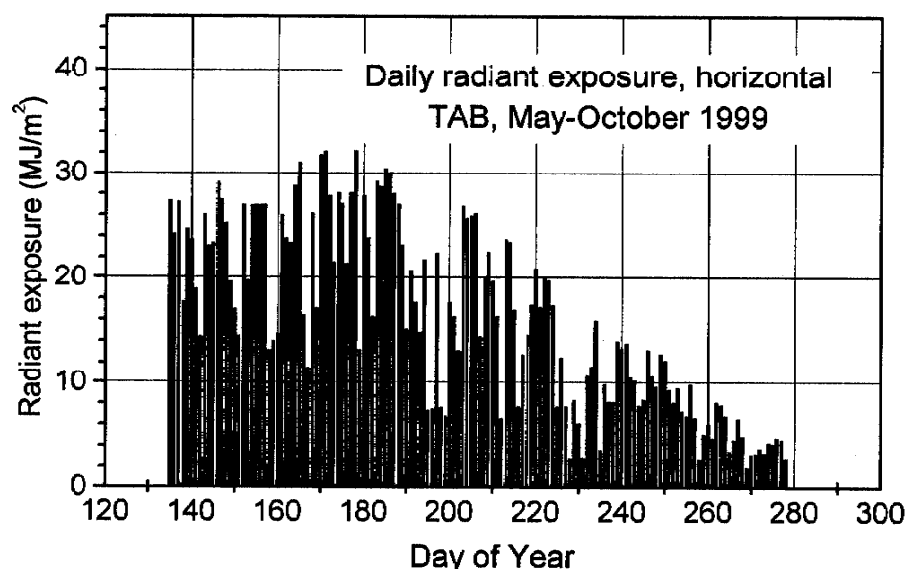


Figure 6.1: The short wave radiant exposure on a horizontal surface was measured using a Yankee Environmental Systems pyranometer.

SELECTION OF REFERENCE DAYS

Our analysis strategy has been to select days with high, continuous levels of direct solar irradiance for in-depth analysis with respect to aerosol optical depth. Although many days are characterized by Langley graphs of apparently high quality, data on partly cloudy days can be expected to be contaminated with undispersed cloud particles which could obscure the aerosols we wish to observe. Figure 6.2 shows examples of two such days.

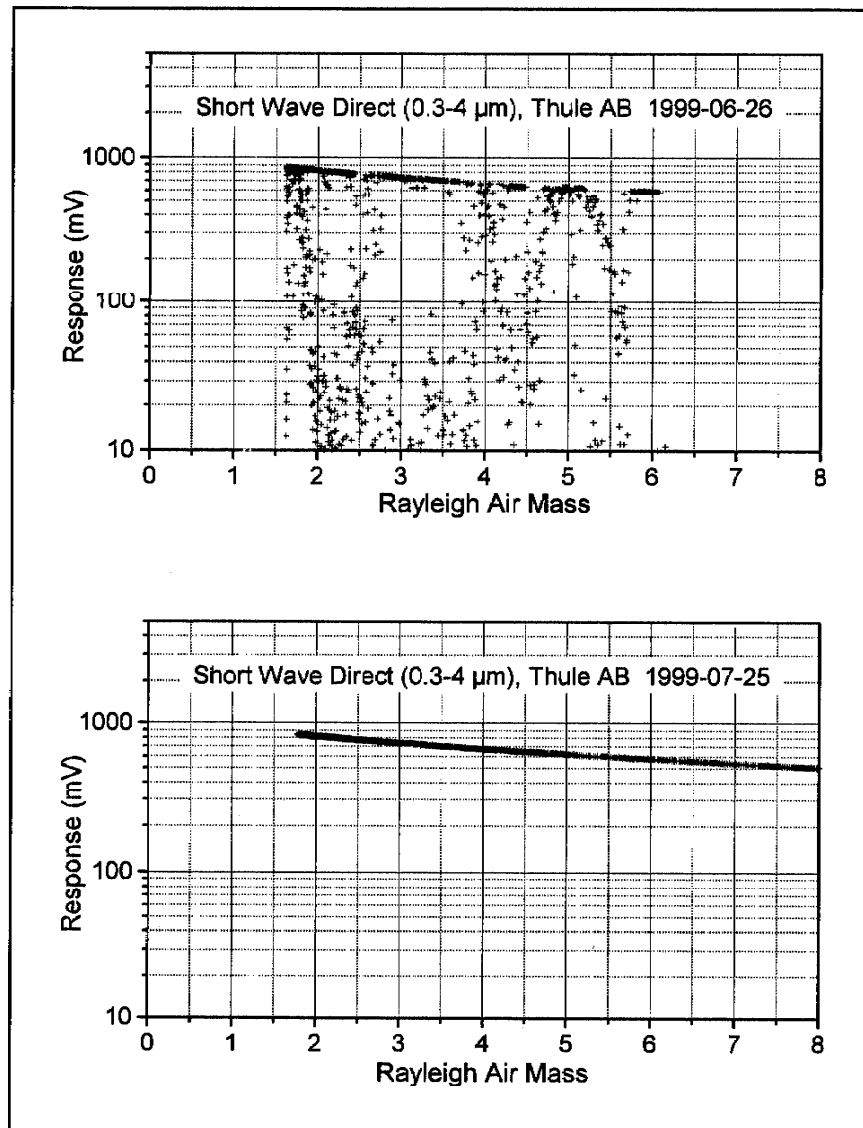


Figure 6.2: *The Langley plot of short wave data from June 26th shows how a convincing Langley graph can be drawn even on a partly cloudy day. The data of July 25th is however better suited to analysis of atmospheric aerosol due to the absence of spurious cloud particles which are often present on days with intermittent sunshine.*

Candidate days of clear, unobstructed observation were selected from the data base by performing the following automated sorting process. Daily short wave radiant exposure values for the horizontal surface were computed along with daily total direct short wave radiant exposure, both quantities in MJ/m².

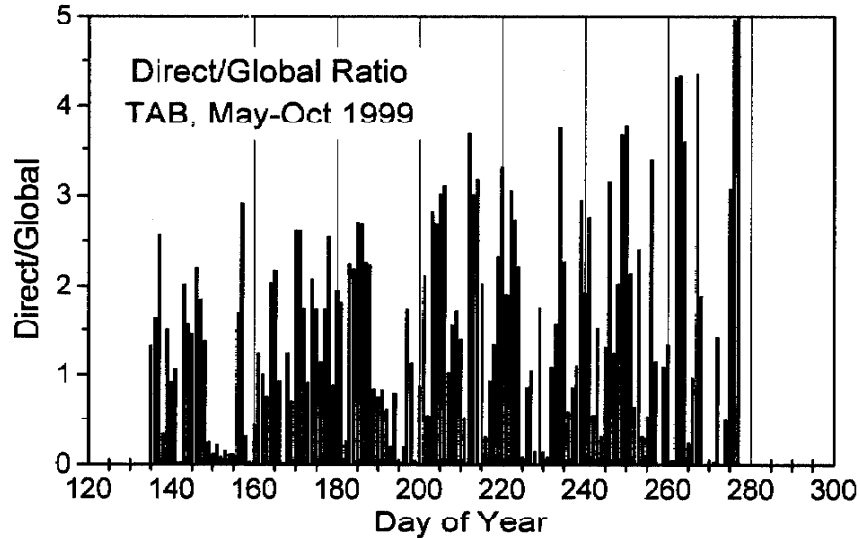


Figure 6.3: Days of each month were sorted to find good direct/global ratios. The best days were selected for analysis.

The ratios of direct to global irradiance were calculated for each day, and days of each month were then sorted to reveal those days with the greatest direct to global ratio. A visual evaluation was then performed to find a reasonable sequence of days covering the period of interest from mid-May through early October. Figure 6.3 shows the computed ratios vs. day number, and Tables 6.1A and B display data for later use.

DATE	Day No.	Direct (MJ/m ²)	Pressure (mB)	Temp. (°C)	SAT	WX
15 May	135	-	979.9	-11.8	App A	App A
25 May	145	34.0	991.2	-9.3	App A	App A
05 Jun	156	-	982.5	-3.4	App A	App A
20 Jun	171	84.1	970.5	0	App A	App A
29 Jun	180	54.3	986.9	0	App A	App A
06 Jul	187	63.5	979.8	0	App A	App A
24 Jul	205	78.4	985.2	0	-	App A
31 Jul	212	24.3	989.3	0	App A	App A

Table 6.1A: Reference day overview TAB, May-July 1999.

DATE	Day No.	Direct (MJ/m ²)	Pressure (mB)	Temp. (°C)	SAT	WX
07 Aug	219	40.7	997.7	0	App A	-
22 Aug	234	59.6	963.6	0	App A	-
27 Aug	239	41.4	974.6	-1.2	App A	-
06 Sep	249	46.8	985.5	-1.6	NA	-
07 Sep	250	45.8	986.3	-1.5	NA	-
19 Sep	262	35.0	989.3	-2.1	NA	-
03 Oct	276	23.8	981.9	-3.5	NA	-
04 Oct	277	22.8	980.3	-3.2	NA	-

Table 6.1B: Reference days TAB, August-October 1999. "Direct" is total direct short wave radiant exposure measured with the broad-band pyrhelimeter, "Pressure" and "Temp." are daily average observed pressure and temperature at the laboratory. The last two columns indicate which days have satellite images or weather maps in Appendix A.

Having selected days for detailed further analysis, the first step is computation of aerosol optical depths. With this information available we can perform inversions to reveal information about aerosol particle size distributions in the Arctic air above Thule Air Base.

OZONE AND NO₂ CORRECTIONS

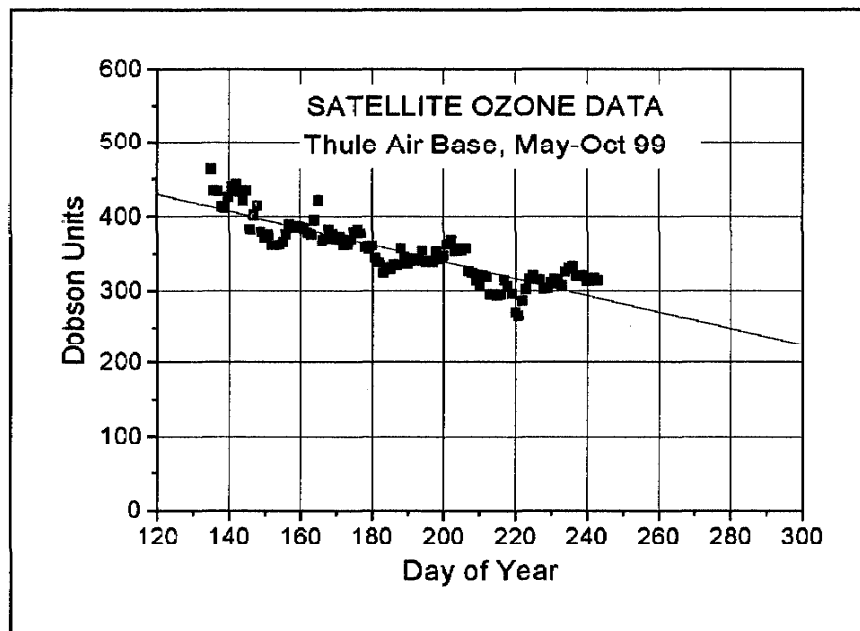


Figure 6.4: TOMS satellite measurements of column ozone values for Thule Air Base, 1999. (Regression: $DU = -1.12 \cdot DAY + 563$)

Determination of aerosol optical depth requires knowledge of the Rayleigh air mass m_R at each of the pyrheliometer wavelengths (368, 500, 1030 and 1550 nm), the ozone air mass, the column ozone value C_{O_3} for Thule Air Base and the *spectral ozone absorption coefficient* K_{O_3} . TOMS (*Total Ozone Mapping Spectrometer*) satellite measurements of column ozone are shown in Figure 6.4 and relevant values are shown in Table 6.2 for the set of reference days selected.

DATE	Day No.	Column ozone (Dobson units)	τ_{O_3} (500 nm)
15 May	135	462	0.01525
25 May	145	434	0.01432
05 Jun	156	376	0.01241
20 Jun	171	372	0.01228
29 Jun	180	360	0.01188
06 Jul	187	334	0.01102
24 Jul	205	353	0.01165
31 Jul	212	318	0.01049
07 Aug	219	296	0.00977
22 Aug	234	325	0.01073
27 Aug	239	320	0.01056
06 Sep	249	284	0.00937
07 Sep	250	283	0.00934
19 Sep	262	270	0.00891
03 Oct	276	254	0.00838
04 Oct	277	253	0.00835

Table 6.2: Satellite data for column ozone at Thule Air Base during May-October 1999 for selected reference days. Actual satellite data was used except for the last days of the season where an extrapolation has been made (Figure 6.4). The ozone absorption coefficient for the 500 nm channel has been set to 0.033 cm^{-1} .

Note that a correction for ozone absorption is required only for the 500 nm channel, since the absorption coefficient is insignificant at 368 nm and for the NIR wavelengths used in this work.

A brief remark is in order concerning the column value of NO_2 at Thule Air Base and the possible influence of NO_2 on the results. Measurements are available from SAOZ (*Système d'Analyse des Observations Zenithales*) developed in France [Pommereau, 1988]. An instrument for performing these measurements has been in place

at the Thule Air Base Laboratory from the autumn of 1990 through the spring of 1999. Analysis performed by Signe Andersen [Andersen, 1998] suggests late spring and early autumn NO_2 column values of about $5 \cdot 10^{15}$ molecules/cm².

It can be helpful to have an overview of the influence of column ozone and NO_2 on optical depth measurements. The ozone and NO_2 molecular absorption cross sections vs. wavelength are therefore shown in Figure 6.5.

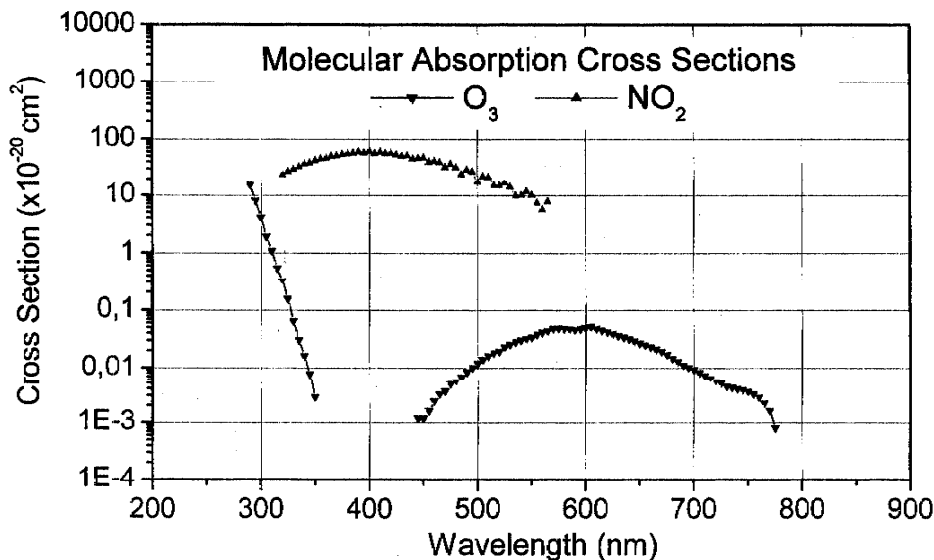


Figure 6.5: Ozone and NO_2 absorption cross sections derived from [Leckner, 1977] and [Harwood, 1994] are shown for 298 K.

Note from Figure 6.5 that the 368 nm channel lies just above the Huggins absorption band (300-350 nm) for ozone, while the 500 nm channel lies within the Chapuis band for ozone in the visible region. Ozone absorption is insignificant for the 1030 and 1550 nanometer channels. The ozone data are derived from [Leckner, 1977, p 144] and are originally due to [Vigroux, 1953]. More recent studies show the same qualitative features with improved accuracy. The NO_2 cross sections are taken directly from [Harwood, 1994, Table 2] and in accord with other sources such as [Seinfeld, 1998, Figure 3.11]. Noting that a stratospheric ozone layer of about 400 DU corresponds to a column content about 10^{20} molecules/cm² and that the column content for NO_2 is about $5 \cdot 10^{15}$ molecules/cm², it is apparent from Figure 6.5 that the optical depths will typically be similar in magnitude. To show this Figure 6.6 shows a comparison of the ozone and NO_2 optical depths which were typical during the period May-October 1999 at Thule Air Base.

Figure 6.6 shows that it is important to take NO_2 into account for both the 368 and the 500 nm channels, while the ozone correction need only be made for the measurements at 500 nm.

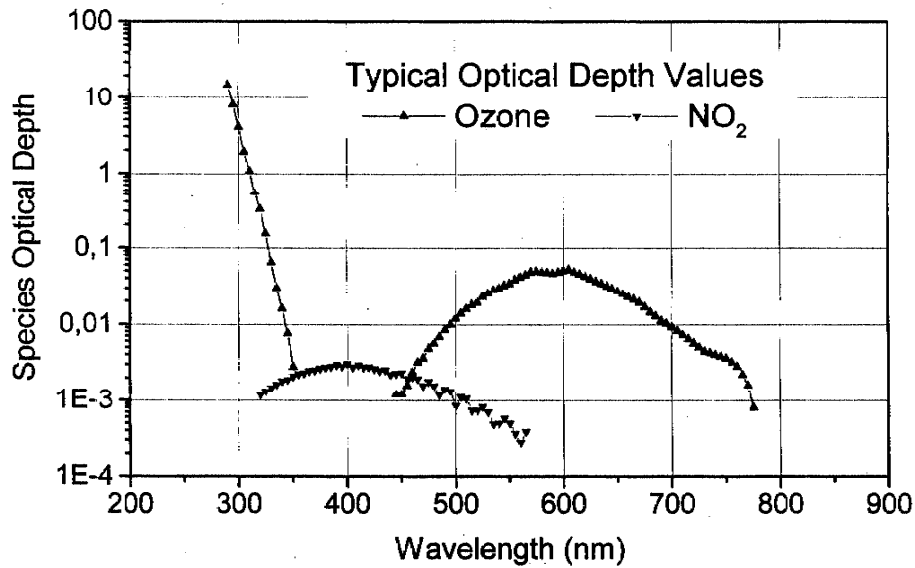


Figure 6.6: Typical ozone and NO_2 optical depths vs. wavelength for Thule Air Base during our experiment (May-Oct 1999).

The relevant data are summarized in Table 6.3:

Wavelength	O_3 absorption (cm^{-1})	O_3 optical depth (for 400 DU)	NO_2 cross section ($cm^2/molec.$)	NO_2 optical depth (for $5 \cdot 10^{15} cm^{-2}$)
368 nm	0	0	$5.38 \cdot 10^{-19}$	0.00270
500 nm	0.033	0.0132	$1.51 \cdot 10^{-19}$	0.00076

Table 6.3: The absorption coefficients for O_3 and NO_2 and typical optical depths for the 368 and 500 nm channels are shown. A value of about 400 DU was typical for ozone, and a column NO_2 content of $5 \cdot 10^{15}$ molecules per cm^2 is assumed.

OZONE AND NO_2 AIR MASS

Because the ozone and NO_2 layers are at high altitude (at about 18 km and 30 km respectively over Thule Air Base) the air masses for these species will be slightly less than the Rayleigh air mass. For NO_2 the correction is small ($< 1\%$) for solar zenith angles less than 60° but increases rapidly for higher zenith angles (3% at 70° and 16% at 80°). For ozone the difference is somewhat less, exceeding 1% for solar zenith angles greater than 65° (1.7% at 70° and 6.8% at 80°). For an observer at elevation h_O the ozone or NO_2 air mass can be expressed as:

$$\frac{R_E + h_L}{\sqrt{(R_E + h_L)^2 - (R_E + h_O)^2 \cdot \sin^2 \theta_z}} \quad (6.1)$$

where θ_z is the solar zenith angle, R_E is the Earth's radius, and h_L is the elevation of the layer of interest [Komhyr, 1989]. In the data handling program the algorithm due to Andrew Young [Young, 1994] has been applied, and the ozone air

mass has also been computed. Due to the small values of the NO_2 optical depths at 368 nm and 500 nm where corrections are necessary, the ozone air mass value has been used in the computations. This expediency causes a negligible error in the final values of the aerosol optical depths.

Young's algorithm is particularly useful in this connection because it provides corrections for atmospheric refraction expressed in terms of the *actual solar zenith angle* θ_z instead of the *apparent solar zenith angle*. The expression used for the Rayleigh air mass is as follows

$$\frac{1.002432 \cos^2\theta_z + 0.148386 \cos\theta_z + 0.0096467}{\cos^3\theta_z + 0.149864 \cos^2\theta_z + 0.0102963 \cos\theta_z + 0.000303978} \quad (6.2)$$

and is reported by Young to deviate by less than 0.001 air masses for air mass values up to air mass 6 with some systematic error anticipated for high air masses.

AEROSOL OPTICAL DEPTHS

Drawing upon the results derived previously in Chapter 4, we have a relationship between the Rayleigh air mass m_p , the instrument response V_0' that would be measured at the top of the atmosphere at the mean Sun-Earth distance and the voltage V_p that would be measured if aerosols were the only cause of extinction:

$$\tau_p(\lambda) = \frac{1}{m_p} [\ln V_0'(\lambda) - \ln V_p(\lambda)] \quad (6.3)$$

From this result it follows that

$$\ln V_p(\lambda) = \ln V_0'(\lambda) - \tau_p(\lambda) \cdot m_p \quad (6.4)$$

If the natural logarithm of $V_p(\lambda)$ is plotted against the Rayleigh air mass m_p , for the data pertaining to a given day, then a straight line with a slope τ_p will result, provided that the aerosol optical depth is constant during the measurement period. Note that the ozone and nitrogen dioxide corrections as well as corrections for Rayleigh scattering at the wavelength considered are all accounted for in this computation. Substantial changes in the atmosphere, e.g. due to the passage of a front which conveys a body of air with a different aerosol content into the region, will cause deviations from the straight line relationship (Figures 6.7-6.10).

When the atmosphere is stable so that the semilogarithmic graph of Equation 6.4 is linear, then the negative slope can be used to determine the aerosol optical depth. If substantial deviation from the linear relationship occur, then momentary values of τ_p can be computed from Equation 6.3. One might choose to do this for particular values of the Rayleigh air mass m_p at specific times during a given day. In the current work we have focussed attention on the average values obtained from the graphs using a range of the lowest Rayleigh air mass values on a given day. Figures 6.7-6.10 show $\ln(V_p)$ vs. air mass graphs for a typical summer day.

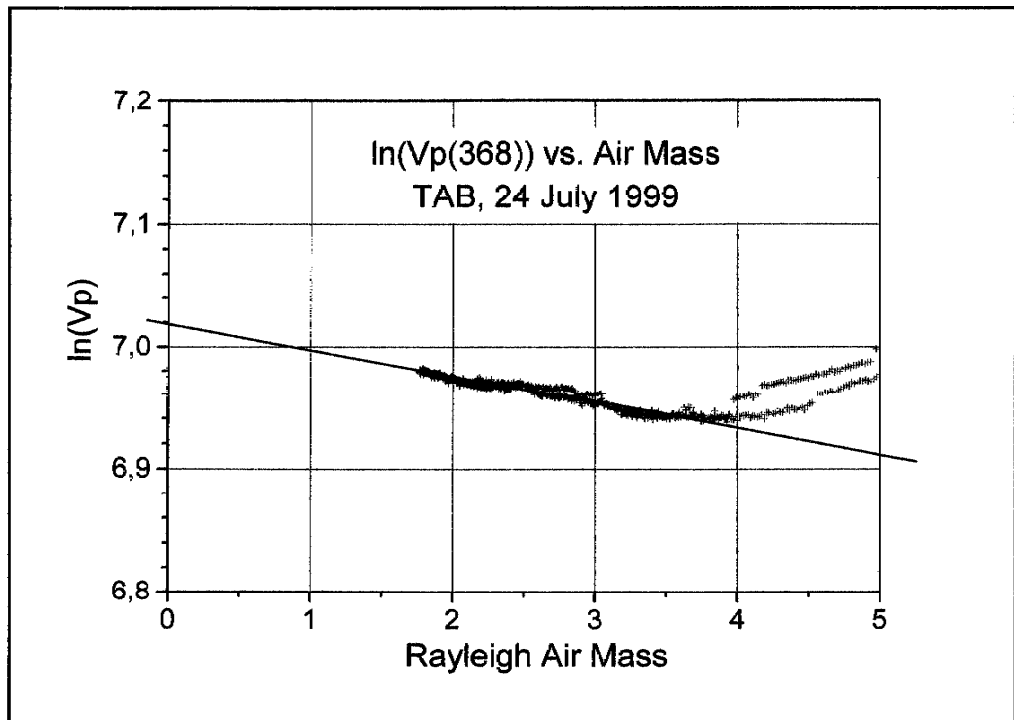


Figure 6.7: Graph of Equation 6.4 for 368 nm data from Thule Air Base on 24 July 1999. The negative slope is the aerosol optical depth.

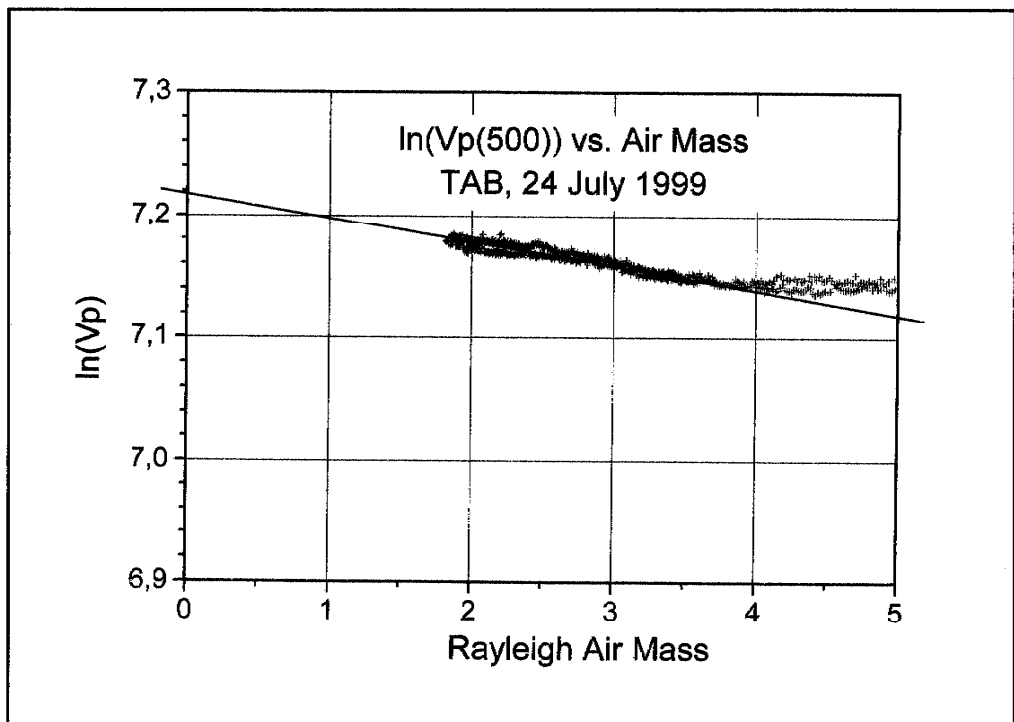


Figure 6.8: Graph of Equation 6.4 for 500 nm data from Thule Air Base on 24 July 1999. The negative slope is the aerosol optical depth.

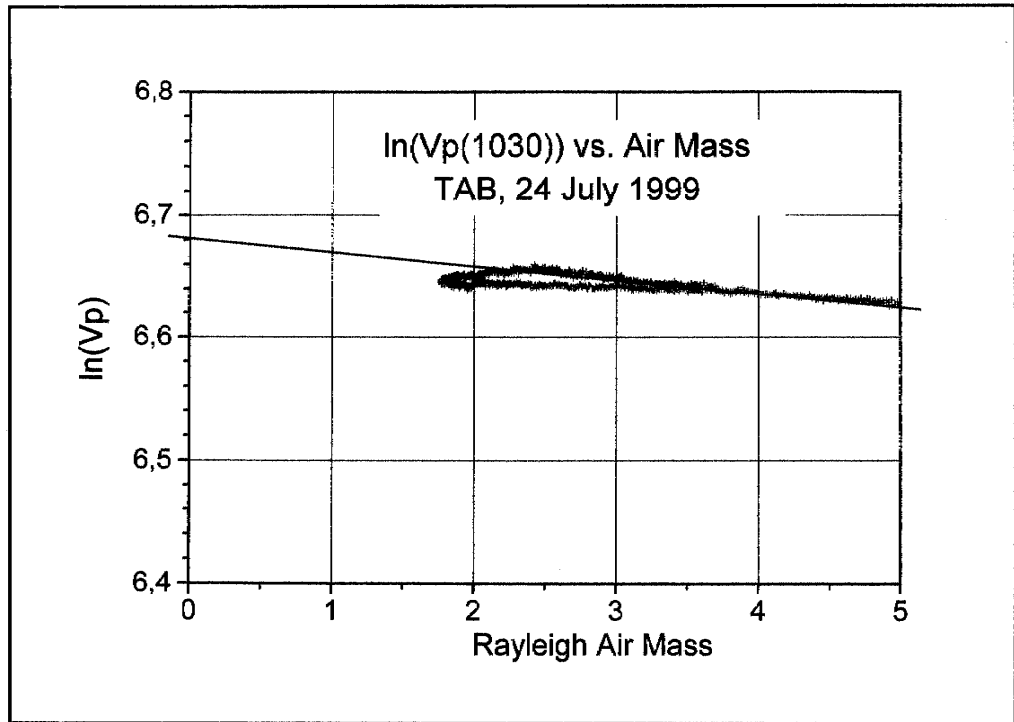


Figure 6.9: Graph of Equation 6.4 for 1030 nm data from Thule Air Base on 24 July 1999. The negative slope is the aerosol optical depth.

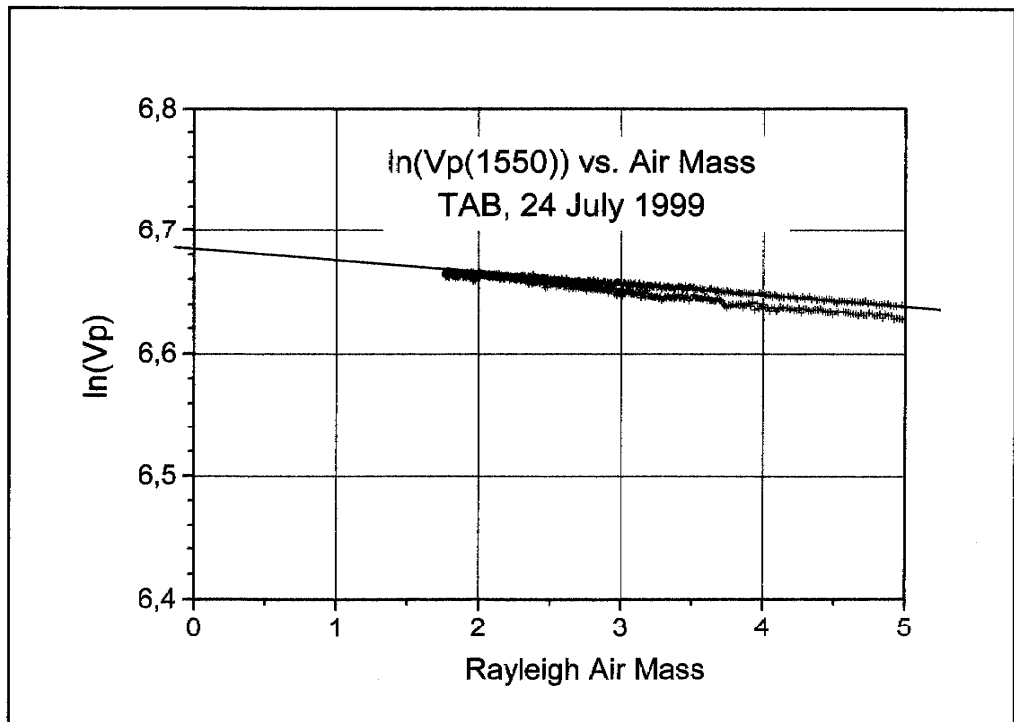


Figure 6.10: Graph of Equation 6.4 for 1550 nm data from Thule Air Base, 24 July 1999. The negative slope is the aerosol optical depth.

Table 6.4 shows the results of this analysis for the period from May 15th through October 4th for the selected reference days. The absolute uncertainty in the optical depth data presented here is about ± 0.003 due to the graphical method employed.

DATE	Day No.	Aerosol 368 nm	Aerosol 500 nm	Aerosol 1030 nm	Aerosol 1550 nm
15 May	135	0.09786	0.06180	0.03250	0.02528
25 May	145	0.02062	0.03000	0.01892	0.01214
05 Jun	156	0.04750	0.03250	0.01278	0.01322
20 Jun	171	0.03964	0.01928	0.01301	0.01046
29 Jun	180	0.01964	0.02072	0.00944	0.01020
06 Jul	187	0.02714	0.02714	0.01250	0.01046
24 Jul	205	0.02964	0.01642	0.00759	0.01049
31 Jul	212	0.02964	0.01430	0.00960	0.01027
07 Aug	219	0.02964	0.01428	0.00793	0.00853
22 Aug	234	0.03358	0.02392	0.01250	0.01072
27 Aug	239	0.03322	0.01356	0.01151	0.01230
06 Sep	249	0.04286	0.03106	0.01115	0.01250
07 Sep	250	0.04214	0.01750	0.01151	0.01230
19 Sep	262	0.05894	0.04034	0.01031	0.01052
03 Oct	276	0.09484	(0.06)	(0.03)	0.01053
04 Oct	277	0.09107	(0.06)	(0.03)	0.00929

Table 6.4: *The measured values of aerosol spectral optical depths at 368, 500, 1030 and 1550 nm at Thule Air Base during May-October 1999 for selected reference days are shown here. These data constitute important "bottom line" results of this work.*

Graphical representations of the data are provided on the following page in Figures 6.11 and 6.12. The waterfall diagram in Figure 6.11 shows the truest representation of the results, for the values plotted are identical to the data of Table 6.4. The 3D surface plot uses an algorithm which tends to even out variations in the data and provides a smoothed result. Note also that the zero optical depth plane in Figure 6.12 has been displaced upwards to permit viewing of the 2D overview diagram below the 3D surface.

It should be emphasized that the results achieved during this single season of measurements at Thule Air Base should be regarded as tentative, and that the apparent increases in aerosol optical depth at the beginning and at the end of the measuring season are also associated with limitations in the range of Rayleigh air mass available to perform the analysis.

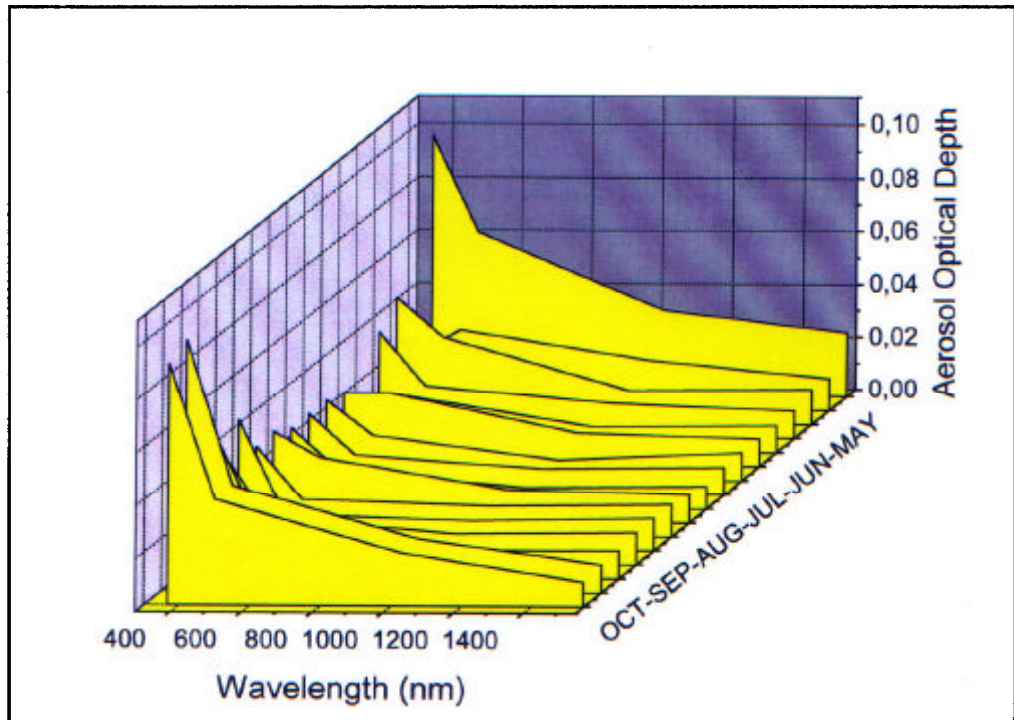


Figure 6.11: *This 3D waterfall graph provides an overview of the aerosol optical depth data presented in Table 6.4.*

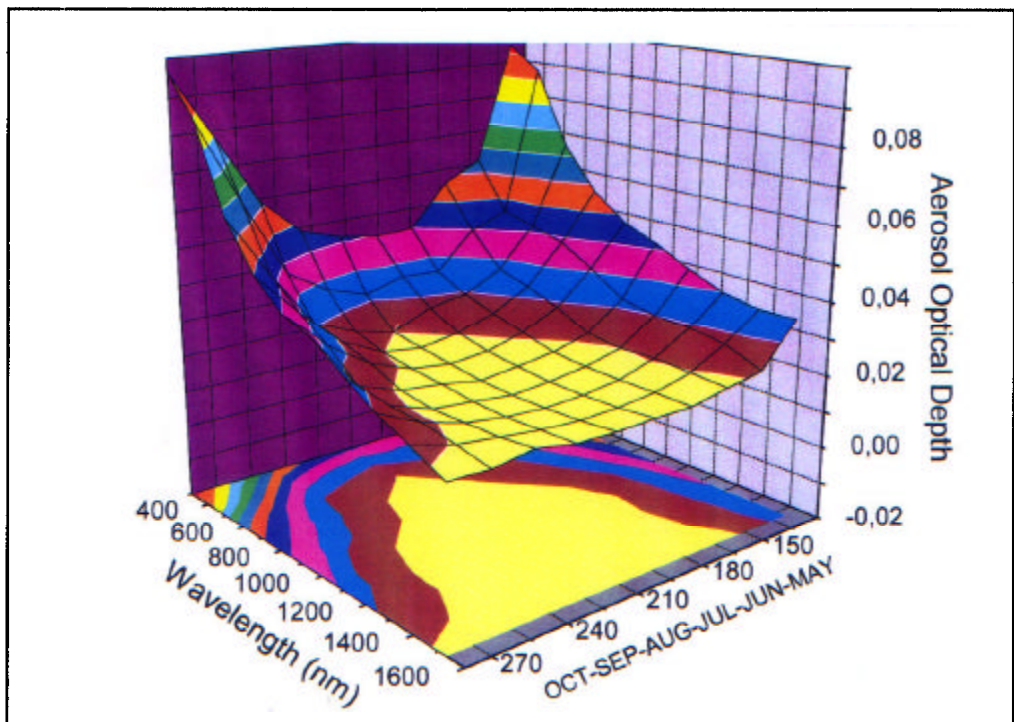


Figure 6.12: *The aerosol optical depth data are presented here in a 3D surface representation to provide an intuitive overview of the results.*

An ideal situation would permit simultaneous airborne sampling at a variety of altitudes in the troposphere in an effort similar to the AGASP (Arctic Gas and Aerosol Sampling Program) initiative carried out in the spring of 1983. This effort combined satellite observations, airborne and surface aerosol sampling as well as optical ground-based aerosol optical depth observations [Schnell, 1984].

It is interesting to examine the aerosol optical depth data for the visible wavelength 500 nm more closely, for such measurements have been performed at other Arctic locations. Figure 6.13 shows the results from Thule Air Base at this wavelength:

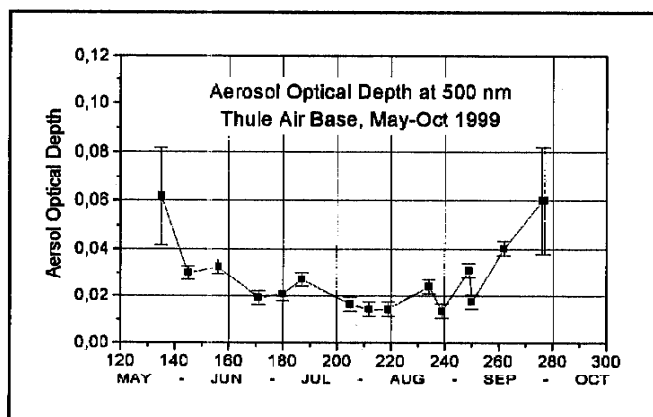


Figure 6.13: Aerosol optical depth at 500 nm from Thule Air Base, May-Oct 1999.

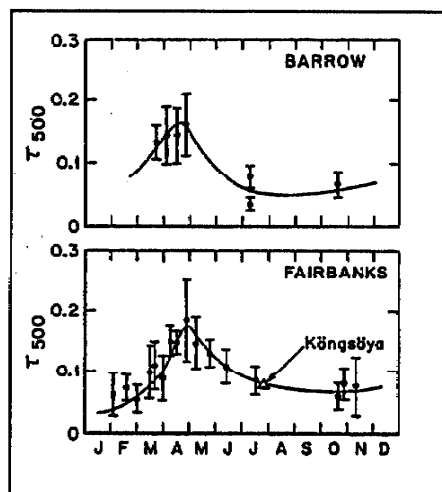


Figure 6.14: Aerosol optical depth (500 nm) at some Alaskan Arctic locations and Köngsöya, Norway.

Similar data for Barrow (71.3°N, 156.7°W) and Fairbanks (64.9°N, 147.9°W), Alaska, are available from [Shaw, 1982], and they are presented in Figure 6.14. A single data point in Shaw's figure is from Köngsöya (78.85°N, 29.30°E), Norway. As can be seen from Figures 6.13 and 6.14 there is good accord between our measurements and Shaw's results. The population concentration near Fairbanks may be responsible for the somewhat higher values of τ_{500} there compared with Barrow. Our measurements suggest that the 500 nm aerosol optical depths at Thule Air Base were even lower. The decreasing trend from during late spring and the increasing trend in autumn seen in Shaw's figure are suggested by our data but uncertain. It will be very interesting to see the results from Thule Air Base during the coming spring months and during the coming measurement season.

Arctic data is also available in the literature for comparison with our results at the near infrared wavelength 1030 nm. E. Becker et al. describe measurements performed using a star photometer during the winter months in conjunction with a solar photometer [Becker, 1999]. The 1000 nm star photometer data reported by Becker for Ny Ålesund was not measured directly but calculated from a range of visible wavelengths by means of the two-star extinction method [Leiterer, 1995] and a method proposed by A. Ångström [Ångström, 1961]. Figure 6.15 shows the 1030 nm aerosol optical depth results from Thule Air Base, and the measurements from Becker et al. can be seen in Figure 6.16.

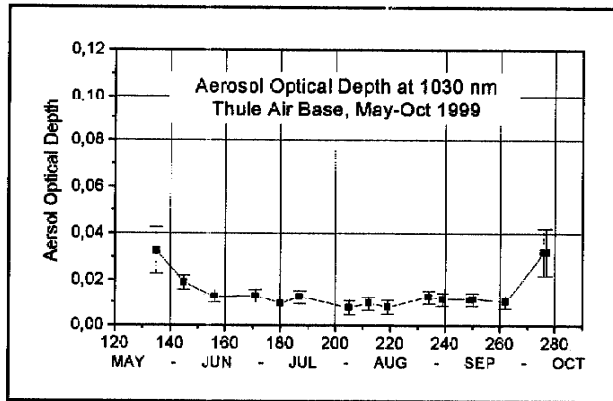


Figure 6.15: Aerosol optical depth at 1030 nanometers at Thule Air Base, May-Oct 1999.

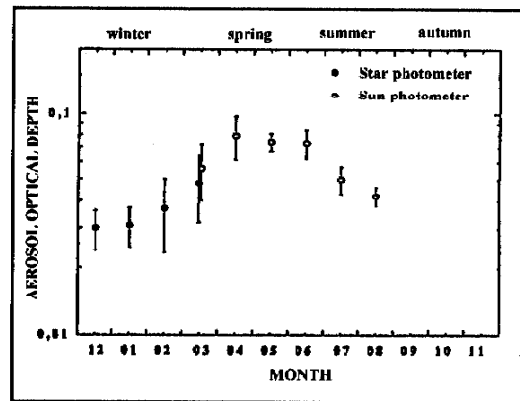


Figure 6.16: AOD at 1000 nm from Ny Ålesund (79°N, 11°E), Norway, 1997.

The 1000 nm values derived by Becker et al. in May - August 1997 in Barrow follow our 1999 measurements from Thule well, including the tendency for declining aerosol optical depth values from May through mid-summer.

SIZE DISTRIBUTIONS

With reasonable values for the aerosol optical depth in hand it is possible to use the analytical tools described in Chapter 4 to perform some inversions and to arrive at some particle size distributions on selected days.

Early and late in the measuring season we observed rather high UV (368 nm) aerosol optical depths monotonically decreasing in a manner similar to the data of Dalu, Rao et al. shown in Figure 4.10. This leads us to try a Junge power law distribution in the inversion integral for the data of September 19th.

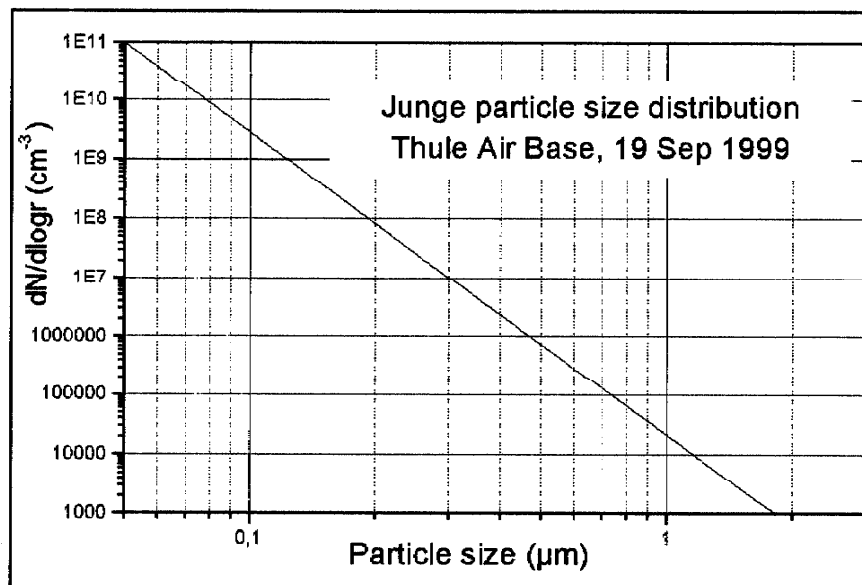


Figure 6.17: This Junge size distribution was inverted from the Thule Air Base data of 19 Sep 1999 shown in Figure 6.18.

The inversion converges in this case with the constants in the power law given by $C = 21328$ and $p = 5.1235$. Figure 6.17 shows the computed size distribution $n(r)$ resulting from the inversion procedure.

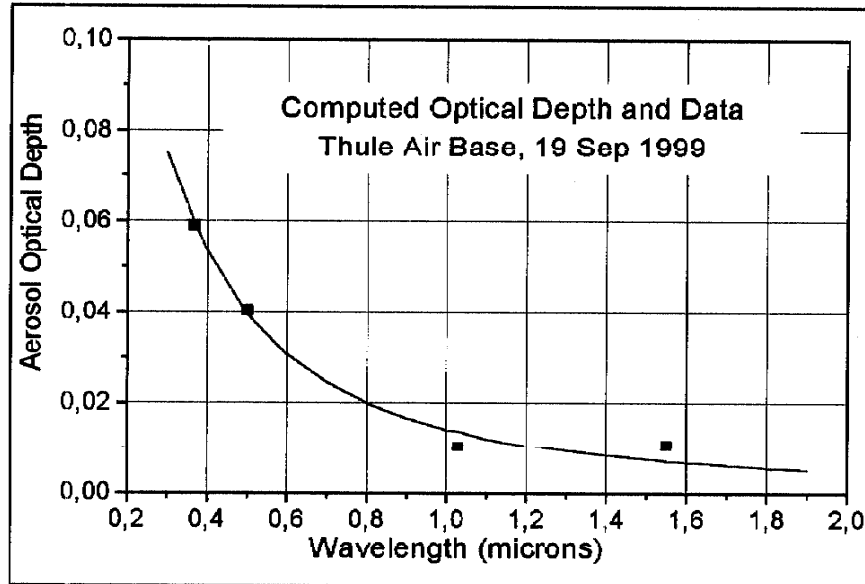


Figure 6.18: The computed aerosol optical depth using $n(r)$ and the measurements from which the 19 Sep 1999 inversion was found.

The measured spectral aerosol optical depths for September 19th are shown as data markers with the function $\tau(\lambda)$ predicted from the inversion in Figure 6.18.

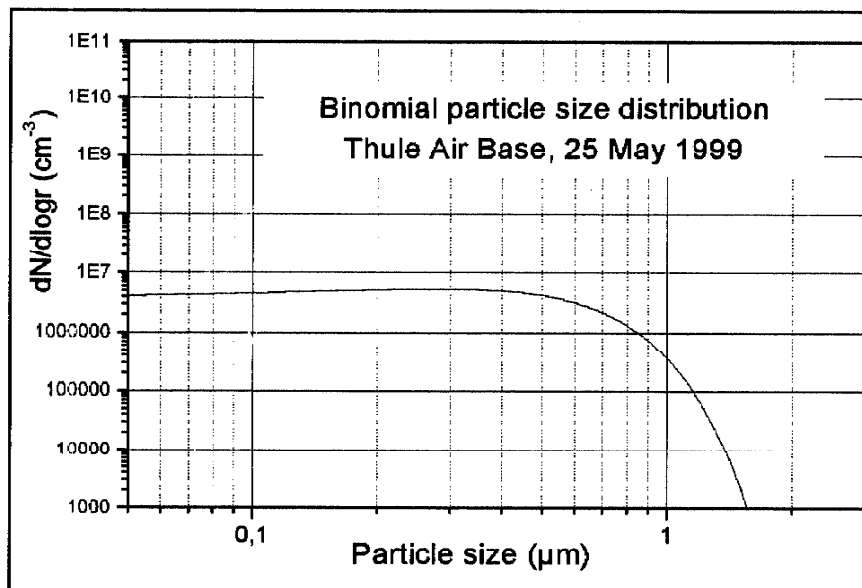


Figure 6.19: This binomial size distribution was used for the Thule Air Base data of 25 May 1999.

The aerosol optical depth data of September 19th was suggestive of Quenzel's data from Figure 4.8 in Chapter 4. Therefore a binomial distribution was used in the

inversion algorithm for this day. Our analytical method was very sensitive to the initial conditions, so that manual experimentation was required to arrive at reasonable initial values for N_0 , r_0 and s_0 (see Equation 4.28).

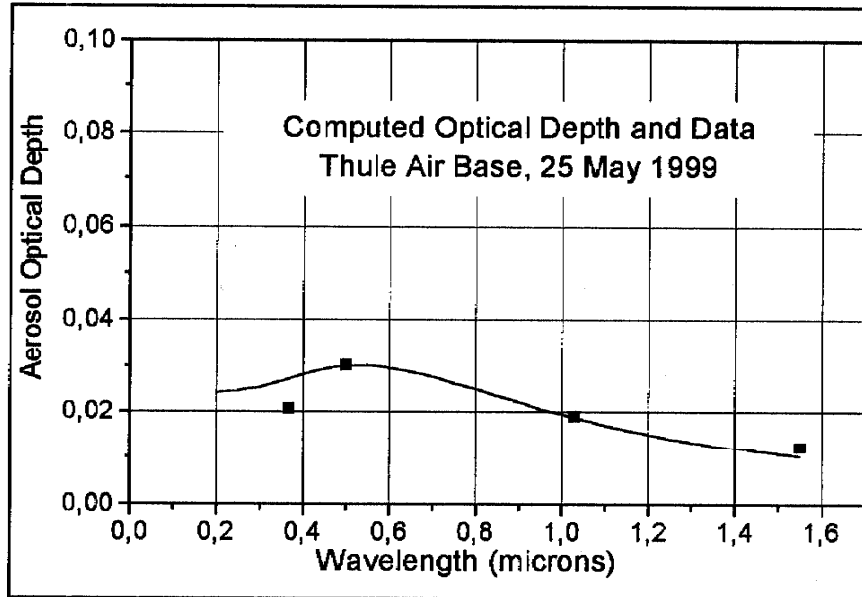


Figure 6.20: Using the binomial size distribution of 6.19 yields the aerosol optical depth shown here. The data are from 25 May 1999.

The function $\tau(\lambda)$ for May 25th computed from Equation 4.23 using the binomial size distribution from the inversion is shown in Figure 6.20.

Note that examination of Figures 6.17 and 6.19 suggests that the size distribution on September 19th consisted of a relatively large number of Aitken particles, while the May 25th distribution was composed primarily of larger particles. The $\tau(\lambda)$ function for May 25th showed a low-end peak suggesting less attenuation in the UV channel than occurred for the September 19th data.

SUMMARY

In this chapter we have reviewed the procedures used to select representative days throughout the summer 1999 measuring season at Thule Air Base. The ozone and NO_2 column contents and air masses have been derived, and correction methods for accounting for the effects of these species on the optical depth measurements have been described. The aerosol optical depth algorithm of Russell et al. has been applied to the data to extract spectral aerosol optical depths for the four observation channels of this experiment.

Finally the algorithms described in Chapter 4 have been applied to the optical depth data to compute aerosol particle size distributions on representative days. Large numbers of small particles can have the same attenuating effect as smaller numbers of large particles leading to some ambiguity in the choice of a size distribution function for use the inversion algorithm.